



DYNAMICAL PROCESSES AT THE VERTICAL CURRENT SHEET BEHIND AN ERUPTING FLUX ROPE

Rui Liu

CAS Key Laboratory of Geospace Environment, Department of Geophysics and Planetary Sciences, University of Science and Technology of China, Hefei, Anhui 230026, China

** To whom correspondence should be addressed. E-mail: rliu@ustc.edu.cn*

Abstract. We report in this paper a solar eruptive event, in which a vertical current sheet (VCS) is observed in the wake of an erupting flux rope in the *SDO*/AIA 131 Å passband. The VCS is first detected following the impulsive acceleration of the erupting flux rope but prior to the onset of a nonthermal HXR/microwave burst, with plasma blobs moving upward at speeds up to 1400 km s⁻¹ along the sheet. The timing suggests that the VCS with plasma blobs might not be the primary accelerator for nonthermal electrons emitting HXRs/microwaves. The initial, slow acceleration of the erupting structure is associated with the slow elevation of a thermal looptop HXR source and the subsequent, impulsive acceleration is associated with the downward motion of the looptop source. We find that the plasma blobs moving downward within the VCS into the cusp region and the flare loops retracting from the cusp region make a continuous process, with the former apparently initiating the latter, which provides a 3D perspective on reconnections at the VCS. We also identify a dark void moving within the VCS toward the flare arcade, which suggests that dark voids in supra-arcade downflows are of the same origin as plasma blobs within the VCS.

1 Introduction

Solar eruptions are the most space weather-relevant energy release phenomena in the heliosphere. They often involve three types of coronal activities: coronal mass ejections (CMEs), flares, and prominence eruptions. These are now generally considered to be different manifestations of a common, but complex, underlying process of destabilization and energy release at active region and even larger scales. The observed close correlation between CME acceleration and flare X-ray emissions in the majority of fast eruptions [e.g., Zhang et al., 2001; Zhang & Dere, 2006; Temmer et al., 2010] implies a mutual feedback between them [e.g., Lin & Forbes, 2000; Lynch et al., 2008].

Theoretically, a vertical current sheet (VCS) is expected to form in the solar corona when a closed magnetic structure is highly stretched due either to the shearing of its footpoints [e.g., Karpen et al., 1995, 2012], or to the catastrophic loss of equilibrium in a magnetic flux rope [Forbes & Priest, 1995; Lin & Forbes, 2000], or, in the classical, “standard” flare model [Kopp & Pneuman, 1976], to a rising filament above the magnetic polarity inversion line. The analytical, two-dimensional model by Lin & Forbes [2000] explicitly predicts the dynamic evolution of the VCS. Specifically, the lower tip of the VCS rises very slowly at a rate constrained primarily by the reconnection rate in terms of the inflow Alfvén Mach

number, while the upper tip of the VCS rises fast at a speed that is only half of the flux-rope rising speed, which results in the formation of a very long current sheet. The formation and similar evolution pattern of the VCS have also been demonstrated in numerical simulations [e.g., Amari et al., 2000; Roussev et al., 2003; Linker et al., 2003], which are based on the same principles as Lin & Forbes [2000] but incorporate much more realistic physics. However, these models do not treat explicitly the physics of the reconnection, which leaves the physical characteristics of the VCS largely unknown, although some progress has been made recently [Ko et al., 2010; Longcope & Bradshaw, 2010; Reeves et al., 2010]. The current sheet formation in CMEs have also been examined in the framework of other models with explicit [e.g., Chen & Shibata, 2000; Shiota et al., 2003] or numerical resistivity [e.g., Karpen et al., 2012].

The positive feedback between the CME and the flare is primarily established via the reconnection at the VCS. In the Lin & Forbes model, the flux rope cannot escape into interplanetary space without some reconnection, due to the tension force associated with the current sheet. On the one hand, the reconnection breaks the field lines that serve to confine the flux rope; on the other hand, it converts magnetic energy into plasma energy. The resultant intense heating creates growing flare loops in the corona and separating flare ribbons in the chromosphere. The reconnection process are also generally thought to play an important role in various nonthermal electromagnetic radiation from gamma-rays, hard X-rays (HXRs) to radio. Three groups of acceleration mechanisms are proposed in the flare context [see the review by Aschwanden, 2006], 1) acceleration by DC electric fields generated in current sheets; 2) stochastic reconnection by AC fields of waves in a turbulent plasma; and 3) shock acceleration. The cusp region of the flare loop has been under intensive scrutiny, where a fast-mode standing termination shock is expected to form when supermagnetosonic jets in the reconnection outflow region, where turbulence is expected to arise, collides with the flare loop [Forbes, 1986]. In addition, particles can be trapped in the cusp region, subject to both betatron and shock acceleration [Somov & Kosugi, 1997].

From the observational viewpoint, the VCS itself might be too narrow to be fully resolved, but the plasma surrounding the current sheet should be visible to a sensitive imaging in-

strument. So far considerable attention has been given to a coaxial, bright ray feature that appears in white light several hours in the wake of some CMEs and lasts from hours to days [e.g., Webb et al., 2003; Ko et al., 2003; Lin et al., 2005]. Along the ray, bright blobs are often observed to flow away from the Sun, suggestive of reconnection outflows [Ko et al., 2003; Lin et al., 2005; Savage et al., 2010]. A few such post-CME rays were studied with UV spectra acquired at 1.5–1.7 R_{\odot} [Ciaravella et al., 2002; Ko et al., 2003; Raymond et al., 2003; Bemporad et al., 2006; Ciaravella & Raymond, 2008], in which the narrow emission of highly ionized ions (e.g., Fe XVIII, Ca XIV) indicates unusually high temperature (3–4 MK) for the corona at that height. Meanwhile, plasma density inside the ray is usually 2 or 3 times larger than the coronal background [Ciaravella et al., 2002; Raymond et al., 2003]. More recently, the VCS was captured in the low corona by imaging instruments such as *SOHO*/EIT [Liu et al., 2010, 2011] and *Hinode*/XRT [Savage et al., 2010]. A major difficulty in the previous studies of current sheets lies in the absence of a narrowband imaging instrument sensitive to hot plasmas above 3 MK, until the recent launch of the Solar Dynamic Observatory [SDO; Pesnell et al., 2012]. The Atmospheric Imaging Assembly [AIA; Lemen et al., 2012] onboard *SDO* offers superior spatial resolution ($1''.2$), temporal cadence (12 s), and wide temperature coverage ($10^5 - 10^7$ K), which makes it possible to detect and track fine structures within flaring current sheets, e.g., plasma blobs were observed to collide or merge with each other before being ejected bidirectionally along the current sheet [Takasao et al., 2012].

An important consequence of the reconnection at the VCS is the retraction of the newly reconnected flux tubes (also termed *field line shrinkage*), which eventually relax into round-shaped post-flare loops. In the earlier studies, the retraction of individual field lines were not directly observed, but were inferred from the heights of flare loops at different temperatures [Svestka et al., 1987; Vršnak et al., 2006]. Vršnak et al. [2006] reported that the shrinkage velocity is 20–30 km s^{-1} at 5 MK, and 5 km s^{-1} at 1 MK. The shrinkage can also be measured from the growth of the post-flare loop system by assuming that the outer edge of the loop system at an earlier time corresponds to the inner edge of the loop system at later times [Forbes & Acton, 1996; Reeves et al., 2008]. It was conjectured that the newly forming reconnected loops are not filled with hot plasma so that they are not observable until they approach an equilibrium state when most of their energy is released and become filled up with hot plasma “evaporated” from the dense chromosphere. Following this thought, it is concluded that the tadpole-like dark voids descending toward the flare arcade at 45–500 km s^{-1} , so called supra-arcade downflows [SADs; McKenzie & Hudson, 1999; Innes et al., 2003; Asai et al., 2004] are actually the cross-sections of evacuated flux tubes retracting from the reconnection site [e.g., McKenzie & Savage, 2009; Sheeley et al., 2004; Savage & McKenzie, 2011]. The magnetic nature of SADs is revealed by quasi-periodic transverse displacements of the dark tadpole tails [Verwichte et al., 2005], which is interpreted as propagating fast magnetoacoustic kink waves. Savage et al. [2010] and Savage & McKenzie [2011] also reported supra-arcade downflow loops (SADLs), which are interpreted as SADs viewed from a perpendicular angle. With

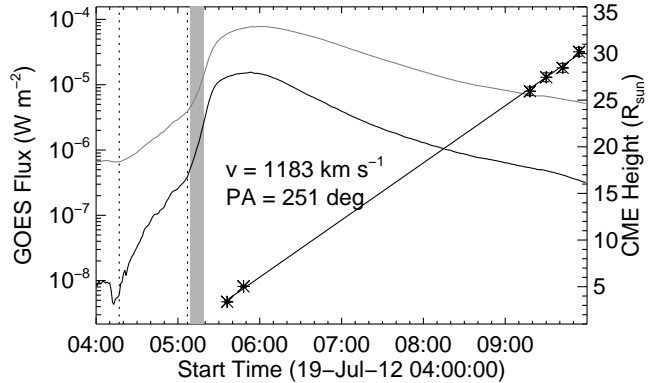


Figure 1: *GOES* 1–8 Å (grey) and 0.4–5 Å (black) flux in relation to the height-time evolution of the CME (asterisks). An error bar of four pixels is assigned for the measurements of the CME height made along the position angle (PA) of 251 deg; only the average CME speed is given by a linear fit due to a data gap of *LASCO* C3 from 05:42 to 09:18 UT. The dashed lines indicate the onset of two flares that convolve together. The grey bar indicates the time interval when the VCS is visible in *AIA* 131 Å during the flare rising phase.

both *STEREO* and *SDO* observations, Warren et al. [2011] concluded that downflows appear as loops or voids that evolve into loops when the flare arcade is viewed face-on, and that only voids are observed when the arcade is viewed side-on. Noticing that the shrinking loops actually lead the voids in a more recent *SDO* observation, Savage et al. [2012] reinterpret SADs as density depletions left in the wake of retracting flux tube. Although SADs are well observed during the gradual phase, against a fan of ‘haze’ above the flare arcade, Asai et al. [2004] and Khan et al. [2007] reported SADs during HXR bursts, using different instruments. Particularly, Khan et al. [2007] found that 73% of downflows start during the SXR flare rise phase, and that 90% of downflows occur during HXR bursts. However, it is not clear whether SADs are linked to HXR bursts in a cause-and-effect fashion or the former occur at all stages of flares so that their temporal co-existence with the latter is a coincidence.

In the section that follows, we present the study of a solar eruption in which a VCS was well observed with *AIA* data. The event generates a wealth of information on the dynamical processes associated with the reconnection at the VCS. In the last section, these observations are discussed in light of models of reconnection and particle acceleration.

2 Observation & Analysis

2.1 Formation of the Erupting Structure

The eruption on 2012 July 19 originated from NOAA AR 11520. It was associated with a long-duration M7.7 flare at S17W91 and resulted in a typical impulsive CME (Figure 1), also known as fast CME. The dynamics of the eruption started from a brightening point at the limb (Figure 2(a); marked by an arrow). A cusp-like loop appeared in emission as early as 04:23 UT. A larger loop appeared simultaneously (Figure 2(b)), connecting the cusp point and the earlier brightening point, which is reminiscent of a “fan” and

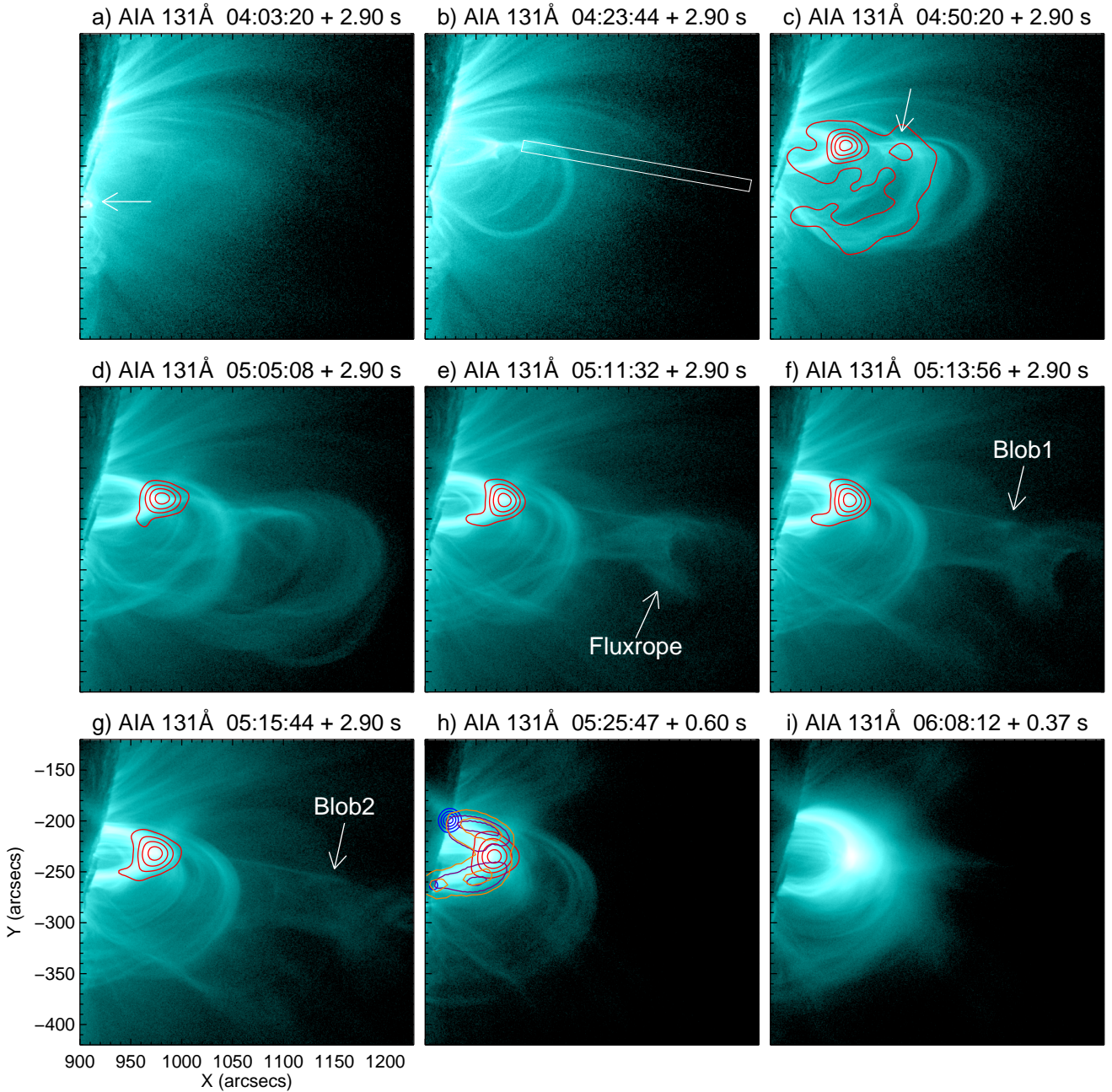


Figure 2: Snapshots of *SDO/AIA* 131 Å images featuring the evolving process of the eruption on 2012 July 19. The exposure time of each image is indicated on the panel caption. Overplotted contours show HXR sources at 6–15 keV (red) and 25–80 keV (blue) reconstructed with the CLEAN algorithm [Hurford et al., 2002], and microwave sources at 17 GHz (orange) and 34 GHz (purple) observed by Nobeyama Radioheliograph (NoRH). The HXR contour levels are 30%, 50%, 70%, and 90% of the maximum brightness of each individual *RHESSI* image except the one overplotted on Panel (c) in which the 10% level is invoked. The microwave contour levels are 30% and 70% of the maximum brightness of each individual NoRH image. In Panels (b) the rectangle indicates the slit used in Figure 5(d). An animation of AIA 131 Å images is available online.

“spine” topology [e.g., Aulanier et al., 2000]. The brightening point corresponds to an separatrix footpoint and the cusp point to a 3D null point in this scenario. This structure was only visible in the AIA hot channels, i.e., 131 Å and 94 Å. The AIA 131 Å channel mainly contains hot lines from Fe Roman20 ($\log T = 7.0$) and Fe Roman23 ($\log T = 7.2$) as well as a cool component from Fe Roman8 ($\log T = 5.6$) [see O’Dwyer et al., 2010, for a comprehensive study of the AIA temperature response]. The AIA 94 Å channel is dominated by hot lines from Fe Roman18 ($\log T = 6.8$) despite cool lines from Fe Roman10 ($\log T = 6.1$). A similar structure appeared in the *RHESSI* HXR image at 6–15 keV integrated over the time interval from 04:49:24 to 04:51:24 UT (Figure 2(c); 10% contour level), which confirms the hot, complex morphology observed in 131 Å. It is natural to assume that the reconnection at the null heated up the plasma at the separatrix fan and spine to ~ 10 MK.

2.2 Formation of the Erupting Structure

It is interesting that in addition to a strong HXR looptop source located at the cusp point there exists a weaker above-the-looptop source ((Figure 2(c); marked by an arrow); both sources could be the product of the reconnection at the null [however, see Liu et al., 2013, for a different interpretation]. As the reconnection process proceeded, quite a few criss-crosses developed among these hot loops (Figure 2(c) and (d)), suggesting the formation of a complicated structure, most likely a flux rope. From a different viewing angle, i.e., the 195 Å channel of the EUVI instrument [Wuelser et al., 2004] onboard *STEREO-A*, one can see the expansion of a group of large-scale loops (Figure 3(a) and (e)), presumably driven by the flux rope. A clear flux-rope geometry appeared after this complicated structure erupted at around 05:07 UT and subsequently exhibited a concave-upward shape at its bottom and a dark cavity inside in AIA 131 Å (Figure 2(e) and (f)). The dark cavity is presumably a manifestation of enhanced magnetic pressure within the flux rope. Correspondingly, the expulsion of the flux rope was seen as persistent dimming above the flare loop from the *STEREO-A* viewing angle (Figure 3(f-h)). The ‘seed’ of the flux rope probably formed during a confined flare seven hours earlier [Patsourakos et al., 2013]. However, the reconnection as evidenced by the cusp-like flare loop prior to the eruption must contribute significant flux to the erupting structure, which results in its destabilization.

An elongated sheet connecting the flare looptop and the bottom of the flux rope was visible in 131 Å from 05:09:32 to 05:19:32 UT (Figure 2(e-g)). This time duration is indicated by the grey bar in Figure 1. Although this is fairly consistent with the expectation from a face-on viewed VCS, the observation is not unambiguous because of the co-existence of various complex structures undergoing dynamic evolution. We argue that this sheet structure corresponds to the VCS behind the erupting flux rope because of the following reasons. 1) It remained as a fairly sharp and straight structure during the detection interval, eventually extending beyond the AIA field of view (FOV). This differentiates it from other linear features within the FOV of interest, which were less extended and soon became either curved or diffused due presumably to the expansion of the eruptive structure. 2) Two blobs of plasma were observed to move upward along the sheet (Fig-

ure 2(f) and (g)) at ~ 680 km s $^{-1}$ and ~ 1400 km s $^{-1}$, respectively (see §2.3.2). This is a distinguishing characteristic of the VCS as revealed in previous studies [Ko et al., 2003; Lin et al., 2005; Takasao et al., 2012]. No moving blobs were detected in any other linear features within the FOV of interest. 3) This sheet structure was similar in location and orientation to the VCS observed later during the gradual phase (Figure 4), which is less ambiguous owing to less complexity involved. 4) The sheet generated no response in any channels other than 131 Å and 94 Å passbands. It was quite diffuse and only marginally visible in 94 Å, due primarily to the relatively poor signal-to-noise ratio in this channel. We hence conclude that the sheet consisted of hot plasma at ~ 10 MK, presumably heated by the reconnection process at the VCS as predicted by the flare/CME theories. This temperature is well constrained, as it is not hot enough to appear in 193 Å, nor cool enough to appear in 335 Å (Fe Roman16; $\log T = 6.4$). The former passband is not only sensitive to Fe Roman12 ($\log T = 6.1$) in the quiet region but also to Fe Roman24 ($\log T = 7.3$) in the flaring region. The sheet disappeared during the nonthermal HXR/microwave burst, suggesting it was further heated to higher temperatures beyond the 131 Å bandpass coverage.

2.3 Dynamics and Timing

We place a virtual slit of 380 by 20 pixels along the VCS in the AIA 131 Å images (Figure 2(b)) to generate a stack plot (Figure 5(d)) in a running-difference approach. Images with longer exposure (2.9 s) are chosen for better visibility of weak structures like the blobs. The white asterisks show the visually picked points along the tracks left by the front and ‘core’ of the erupting structure. The front is fitted with a linear function and a 2nd order polynomial piecewise, and the core with a 2nd order polynomial. Both are labeled by resultant velocities in km s $^{-1}$ and accelerations in m s $^{-2}$. One can see that the erupting structure rose slowly at ~ 30 km s $^{-1}$ from 04:30 UT till 04:50 UT and then began to accelerate at ~ 40 m s $^{-2}$. The acceleration of the core, i.e., the flux rope, increased drastically at about 05:07 UT by an order of magnitude to ~ 600 m s $^{-2}$. The white ‘x’ symbols indicate visually picked points along the tracks left by the two blobs, shifted to the left and right by 1 minute, respectively. The blob velocities obtained with linear fits are ~ 680 km s $^{-1}$ and ~ 1400 km s $^{-1}$, respectively. The tracks left by the blobs converge with the track of the flux rope, indicating that the reconnection outflow associated with the blobs were faster than the erupting flux rope.

It is noteworthy that the *GOES* lightcurve exhibits a significant change of slope at about 05:07 UT before the major peak (Figure 1), suggesting that there might be two flares “convolving” together. Thus, it is no coincidence that the rapid acceleration of the erupting structure, the downward motion of the HXR looptop source as measured by its centroid position, and a hardening of the HXR spectra (Figure 5(b)), i.e., an increase in the (negative) power law index, all onset at roughly the same time. However, the nonthermal (above 25 keV) HXR burst did not start until about 05:15:40 UT, and the footpoint source was not visible in *RHESSI* images until about 05:18 UT, when a microwave burst observed by Nobeyama Radio Polarimeters (NoRP) also commenced (Figure 5(c)). By that time, both blobs have moved out of

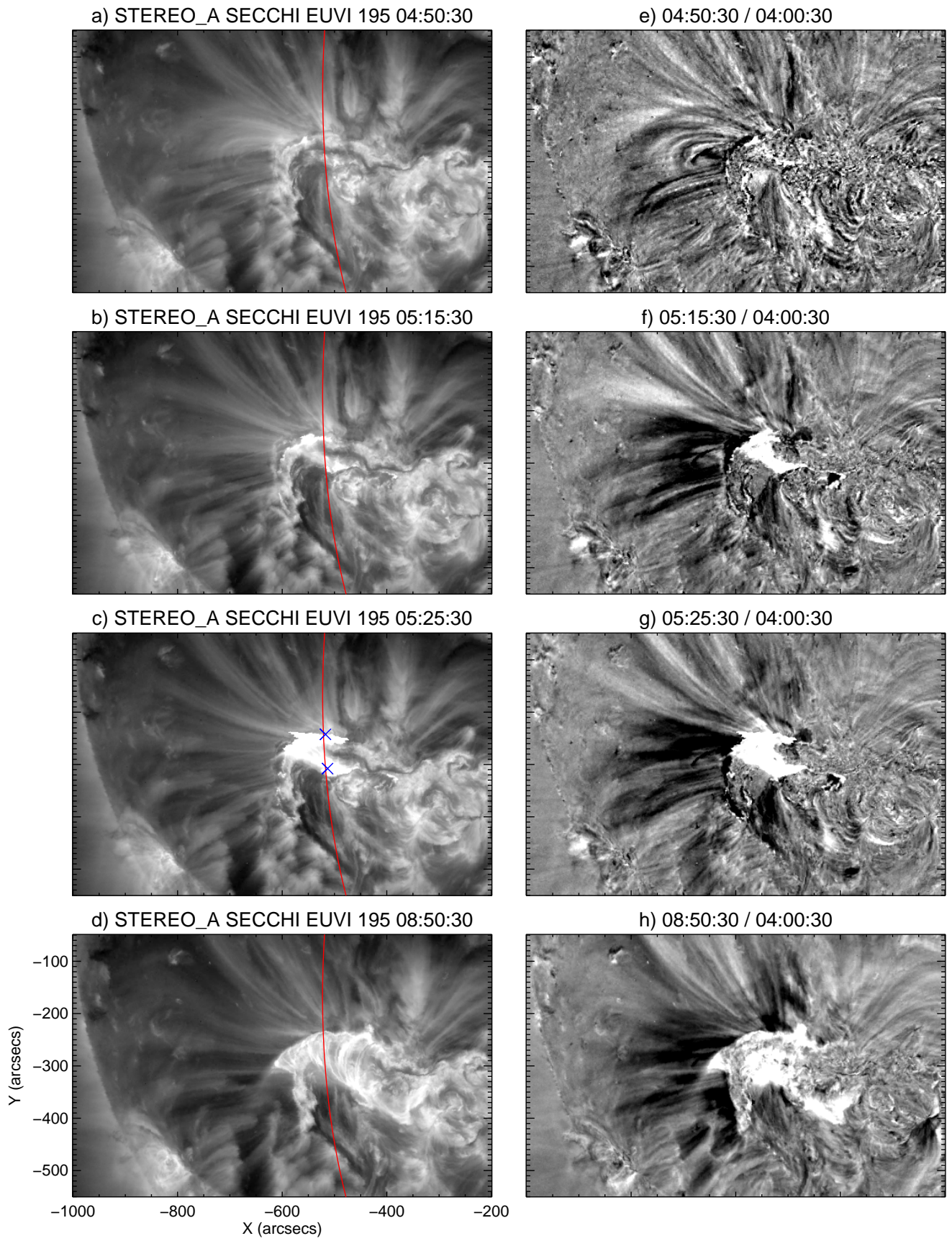


Figure 3: Snapshots of *STEREO-A*/EUVI images (left column) and the corresponding base-ratio images (right column). The red curve delineates the solar limb as seen from *SDO*. In Panel (c), the centroid position of the HXR footpoints are marked in 'x' symbols.

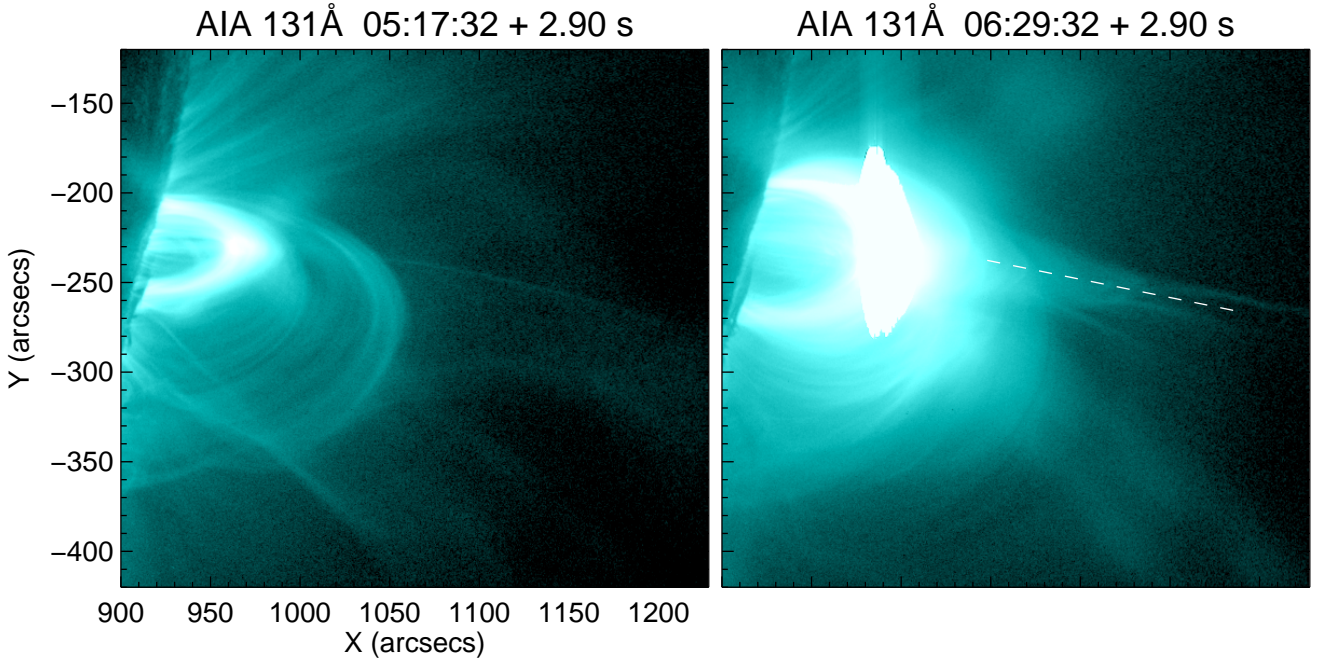


Figure 4: VCS observed during the flare rising phase (left) side by side with the VCS observed during the gradual phase (right). The dashed line in the right panel indicates the location of the VCS in the left panel.

the AIA FOV.

It is remarkable that the microwave emission at 17 GHz and 34 GHz observed by Nobeyama Radioheliograph (NoRH) were concentrated on the legs of the flare loop, which complemented the HXR looptop and footpoint sources to trace out the whole flare loop (see Figure 2(h) and Figure 6). From the bottom panels of Figure 6 which show spectral indices derived from 17 GHz and 34 GHz images, one can see that the microwave emission at 17 GHz and 34 GHz was dominated by optically-thin synchrotron radiation from nonthermal electrons trapped in the flare loop. This substantiates that it is the same population of energetic electrons produced both the HXR and microwave burst, which onset at approximately the same time (Figure 5).

2.4 Field Line Shrinkage and Supra-Arcade Downflows

Both field line shrinkage and supra-arcade downflows were observed in this single event due primarily to the unique orientation and evolution of the flare arcade. Initially, the flare loop was observed in a face-on view and only one sheet structure above the flare loop was observed; but later on, the flare loop began to spread horizontally, presumably along a curved neutral line, to form a flare arcade, which is clearly seen from the *STEREO-A* viewing angle (Figure 3(d) and (h)). To the west of the initial flare loop, the arcade curved southward, which provides *SDO* a side-on viewing angle. As a result, at least three VCS/cusp structures became visible (see Figure 7 and Figure 9). The face-on view is optimal for the observation of flare loop dynamics while the side-on view optimal for that of supra-arcade downflows. A combination of the two viewing angles provides us a 3D perspective.

Successive retractions of individual cusp-like flare loops were observed in the AIA 131 Å channel from about 05:50

to 07:00 UT, and numerous episodes of supra-arcade downflows from about 06:20 UT onward till the end of the flare. Figure 7 shows an example of field line shrinkage. From 06:23:08 to 06:24:44 UT, one can see a small blob moving downward along the current sheet toward its lower tip (or reverse Y-point); at 06:24:44 UT, the blob arrived at the Y-point, and then from 06:25:08 to 06:26:44 UT, one can clearly see a loop retracting from the cusp region. The downward moving blob and the retracting loop left a continuous trajectory on the stack plot (marked by a green arrow on the bottom panel of Figure 8), which is generated from a 280×15 pixel slit intersecting the flare loop system (Figure 7(a)). The trajectory indicates a decelerating process with the blob moving downward faster ($\sim 400 \text{ km s}^{-1}$) than the loop retraction ($\sim 200 \text{ km s}^{-1}$). The latter speed matches the initial speed of field line shrinkage calculated by Lin [2004] using Kopp-Pneuman-type magnetic configurations. Meanwhile, another blob moved downward toward the Y-point from 06:25:56 to 06:26:44 UT (marked by red arrows in Figure 7), which caused transverse displacements of the current sheet in a way similar to the propagation of transverse waves, reminiscent of the wiggling of tadpole tails observed in SADs [Verwichte et al., 2005]. The blob arrived at the Y-point at 06:27:08 UT, apparently initiating another episode of field line shrinkage from 06:27:56 UT onward (marked by a black arrow in the bottom panel of Figure 8). These dynamical processes are difficult to recognize in still images but more readily identifiable in the high-cadence movie accompanying Figure 7.

Among the numerous occurrences of SADs [see Liu et al., 2013, for a comprehensive study], we concentrate here on one single episode occurred at about 06:26 UT, in which the relevant current sheet was located in the further south, well separated from other sheet structures above the flare arcade,

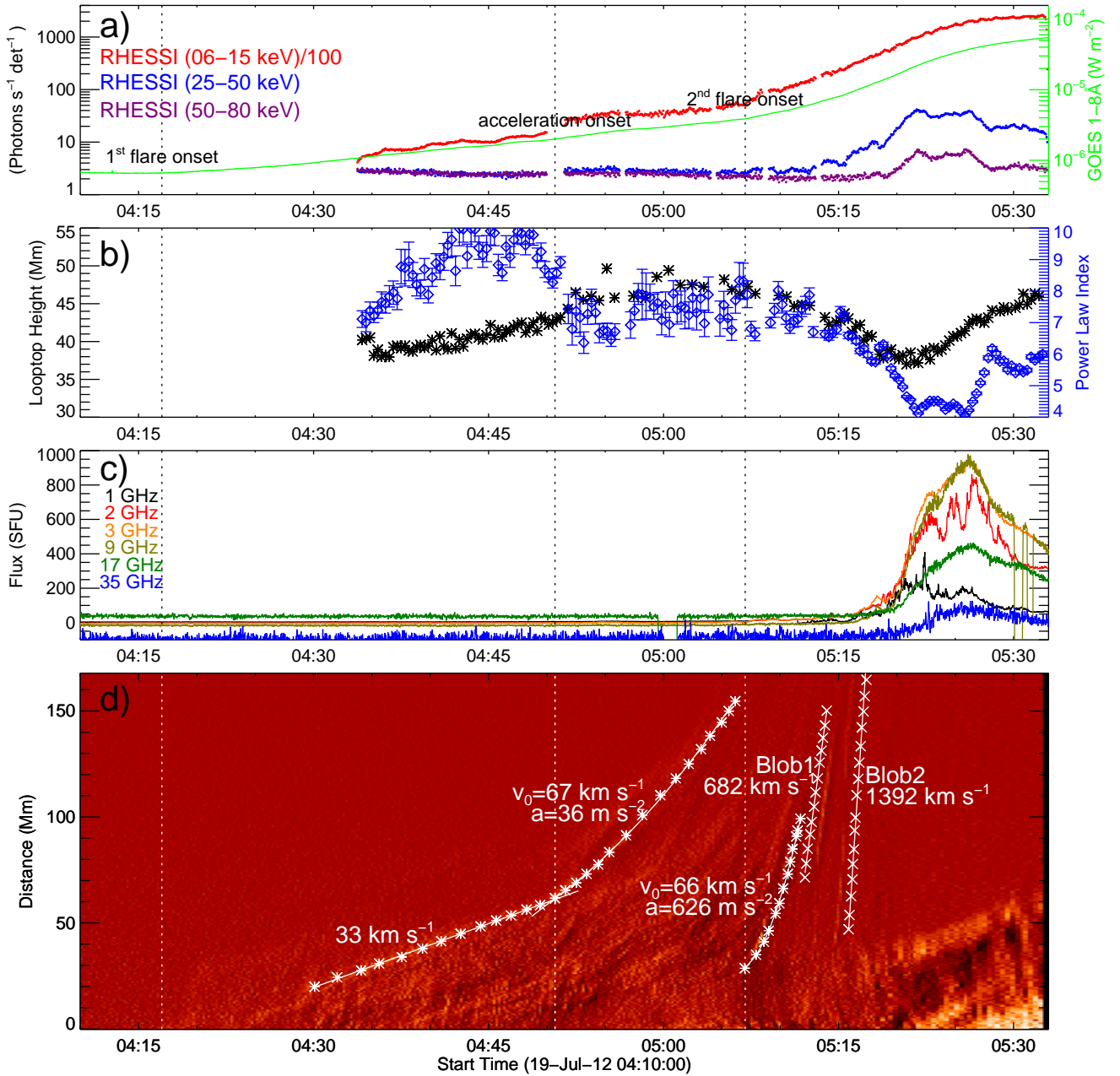


Figure 5: Temporal evolution of the eruption. Panel (a): scaled by the left y-axis are *RHESSI* HXR lightcurves at 6–15 keV (red), 25–50 keV (blue) and 50–80 keV (purple); scaled by the right y-axis is the *GOES* 1–8 Å flux (green). Panel (b): scaled by the left y-axis is the height of the looptop source at 6–15 keV with respect to the middle of two conjugate footpoint (see Figure 2(h)); scaled by the right y-axis are *RHESSI* spectral indices obtained by fitting HXR spectra with an exponential thermal function and a broken power-law function with the spectral index below the broken energy fixed at 1.5. Panel (c): lightcurves (background subtracted) of microwave emission obtained by the Nobeyama Radio Polarimeters. Panel (d): dynamic evolution in 131 Å as seen through the slit in Figure 2(b) (see the text for details). The stack plot without fitting results is available online.

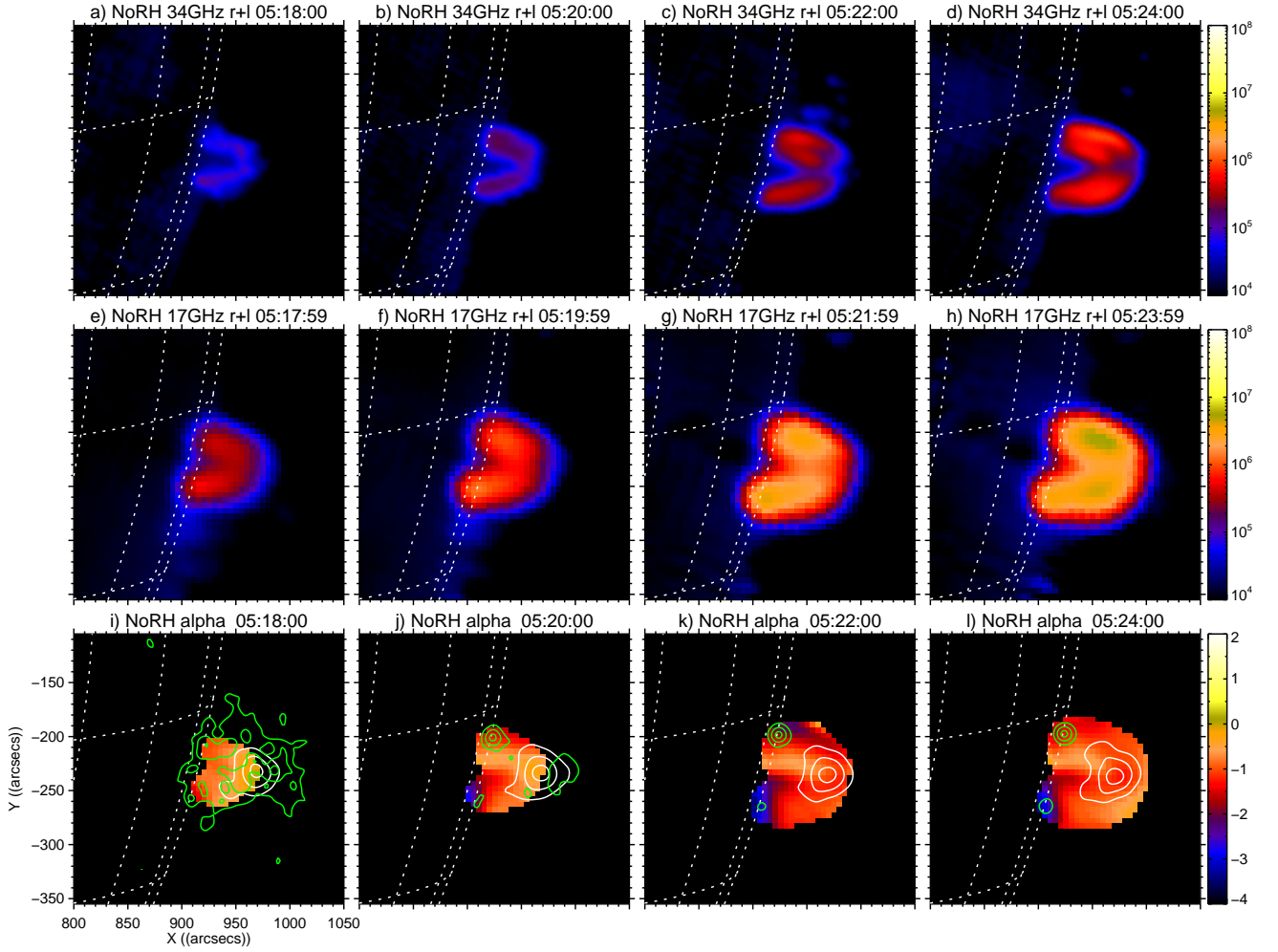


Figure 6: Microwave and X-ray imaging during the impulsive phase of the flare. Top and middle rows show the brightness temperature of microwave emission at 17 GHz and 34 GHz, respectively; The bottom row show spectral indices, α , derived from 17 GHz and 34 GHz images, assuming the observed flux $F_\nu \propto \nu^\alpha$. Overlaid are *RHESSI* contours at 6–15 keV (white) and 25–80 keV (green). The contour levels are 30% and 60% and 90% of the maximum brightness of each individual *RHESSI* image.

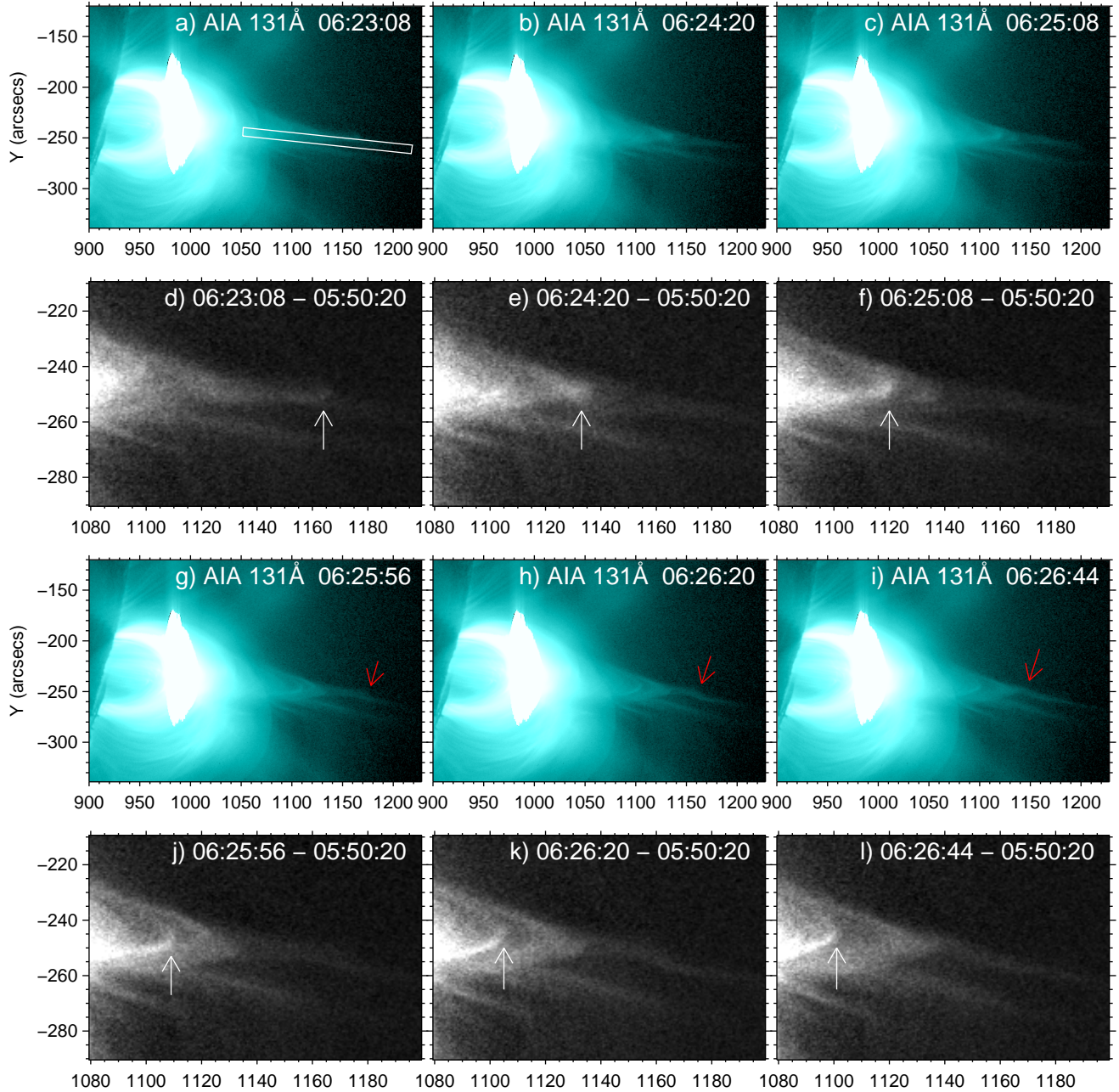


Figure 7: Field line shrinkage as observed in the AIA 131 Å passband. 2nd and 4th row show base difference images with a smaller FOV. Panel a) shows the slit used to generate the stack plots in Figure 8. A blob moving downward along the current sheet and the subsequent field line shrinkage is marked by white arrows. Another blob moving downward along the current sheet which caused apparent transverse displacements of the current sheet is marked by red arrows. An animation of AIA 131 Å images is available online.

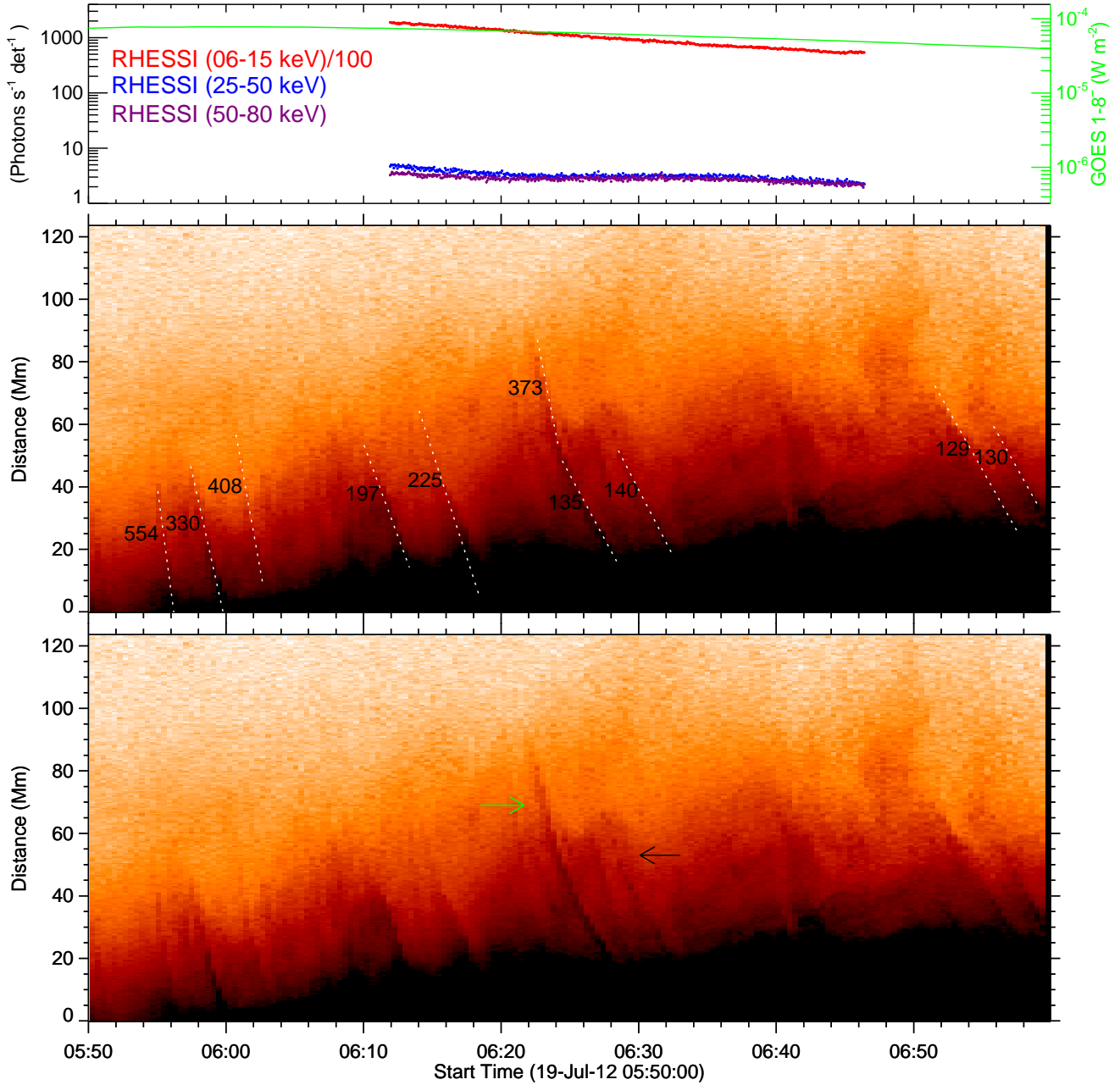


Figure 8: Temporal evolution of downward-moving blobs and field line shrinkage. Top panel shows the *RHESSI* and *GOES* lightcurves in the same format as in Figure 5(a). Both middle and bottom panels show the dynamic evolution in 131 Å as seen through the slit in Figure 7(a), in a reversed, logarithm scale with enhanced contrast, whereas in the middle panel dashed lines indicate linear fits of various tracks, labeled with the resultant speeds in km s^{-1} . The two tracks left by blobs and shrinking loops as shown in Figure 7 are marked by a green and white arrow in the bottom panel, respectively. The stack plot without fitting results is available online.

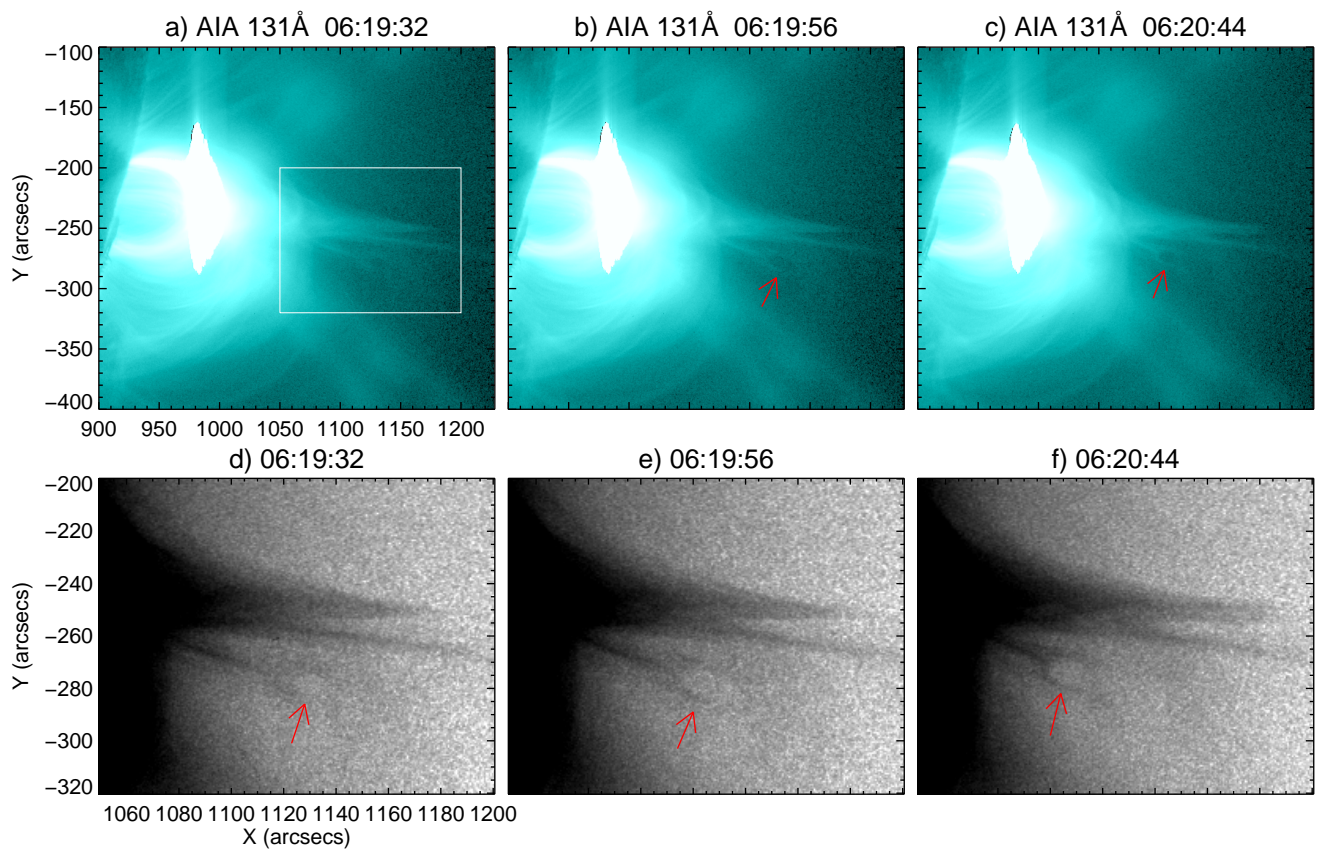


Figure 9: A dark void of supra-arcade downflow as observed in the AIA 131 Å passband. The rectangular region as marked in Panel (a) are shown in the bottom panels with reversed colors. The dark void is marked by red arrows.

so that its relation to the SAD is more clear. In Figure 9 one can see that a blob of dark void (marked by arrows) moved into the current sheet at $\sim 200 \text{ km s}^{-1}$ (please note in the bottom panels the colors are reversed), ending up being surrounded by the hot plasma within the current sheet.

3 Summary & Discussion

3.1 Production of Nonthermal HXR & Microwaves

We investigate the solar eruption on 2012 July 19, in which a VCS forms following the impulsive acceleration of the erupting structure but prior to the onset of the nonthermal HXR/microwave burst. Two blobs are observed to move upward along the VCS at high speeds up to 1400 km s^{-1} . The onset of the nonthermal HXR/microwave burst is delayed by at least 6 minutes relative to the detection of the VCS/blobs (Figure 5). The timing suggests that the VCS with blobs might not be the primary accelerator for nonthermal electrons.

One caveat to keep in mind is that the southern HXR footpoint seems to be partially occulted by the solar limb (see Figure 2(h)), which may affect the HXR lightcurve considering the limited sensitivity of *RHESSI*. However, we have demonstrated that the HXR in this case had a close spatio-temporal relationship with the microwave emission, the latter of which was not subject to occultation, being concentrated on the legs of the flare loop. Hence, we conclude that the effect of the partial occultation is ignorable.

3.2 HXR Looptop Source

It is remarkable that the initial, slow acceleration of the flux rope is associated with the slow elevation of a thermal looptop HXR source and the subsequent, impulsive acceleration is associated with the downward motion of the looptop source (Figure 5). This suggests that the downward motion of the HXR looptop source results from a catastrophic release of magnetic free energy in corona. It is also interesting that the VCS is detected at approximately the same time as the height of the looptop source starts to decrease. These connections might manifest a ‘talk’ between the flux rope in the high corona and the flare loop in the low corona via the VCS, through which a positive CME/flare feedback is established.

The downward motion of the HXR looptop source has been reported in several flares [Sui & Holman, 2003; Sui et al., 2004; Liu et al., 2004, 2009; Veronig et al., 2006; Ji et al., 2004, 2006, 2007; Joshi et al., 2009; Liu et al., 2009]. Some of these flares [Liu et al., 2004; Veronig et al., 2006; Joshi et al., 2009; Liu et al., 2009] are quite similar to the event studied here, i.e., prior to the nonthermal HXR burst the flare has a gradual rising phase dominated by coronal thermal emission, during which the downward motion of the looptop source is observed. Previous studies, however, are focused on the flare itself and interpret this phenomenon in terms of the collapsing magnetic trap model [Veronig et al., 2006], the onset of fast magnetic reconnection Sui et al. [2004] and the relaxation of the sheared magnetic field [Ji et al., 2007]. This phenomenon is now put in

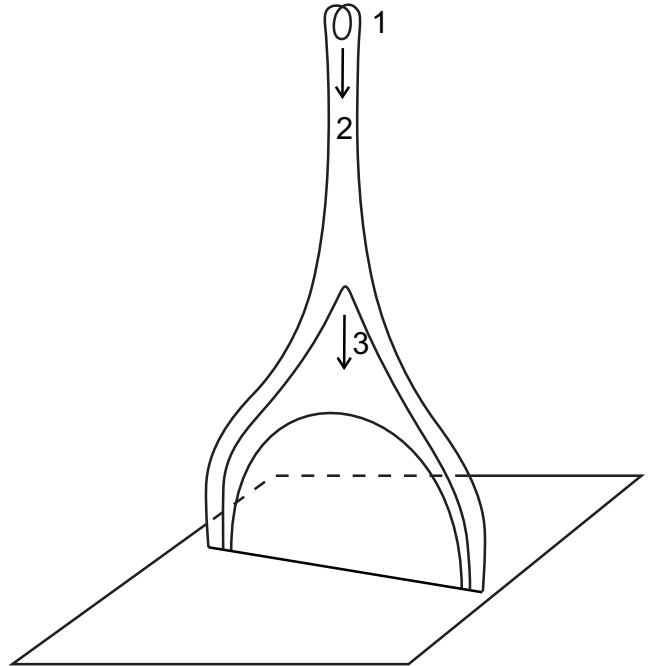


Figure 10: A cartoon illustrating the relationship between the downward moving blob and the field line shrinkage. The numbers indicate three evolving stages, i.e., 1) the formation of a mini flux rope at the top of the reconnected flux tube; 2) the highly stretched reconnected flux tube evolves into a cusp-like flare loop with the twist of the mini flux rope transported away via Alfvén waves; and 3) the cusp-like flare loop evolves into a round-shaped post-flare loop.

the global picture of solar eruptions with this new observation.

3.3 Field Line Shrinkage

This event reveals a close spatio-temporal relationship between the blobs within the VCS moving into the cusp region and the flare loops detached from the cusp region, which leaves a single continuous trajectory in the height-time stack plot (see Figure 7 and Figure 8). With the presence of the VCS and the cusp structure, our observation suggests a evolution sequence involving three stages (Figure 10): 1) A plasma blob forms within the VCS as a mini flux rope with intertwined and entangled field lines via 3D magnetic reconnections. 2) The highly stretched reconnected flux tube evolves into a cusp-like flare loop when the blob moves downward into the cusp region. Alfvén waves are expected to propagate along the flare loop legs toward the chromosphere due to a concentration of twist at the flare looptop. Thus, the blob would shrink and eventually disappear with diminishing twist. This provides a way to transport flare energy to the lower atmosphere as conjectured by Fletcher & Hudson [2008]. 3) The cusp-like flare loop retracts from the cusp region and transforms into a round-shaped post-flare loop, which is the conventional field line shrinkage.

3.4 Supra-Arcade Downflows

The traditional interpretation identifying the dark void in SADs as the cross-section of a shrinking loop [e.g., McKenzie & Savage, 2009; Savage & McKenzie, 2011] has difficulty in explaining the following observational facts:

1. the difference in emissivity between dark voids and bright shrinking loops. This was suggested to be due to the different line of sight with respect to the flare arcade [Savage & McKenzie, 2011; Warren et al., 2011], but the new observation featuring the co-existence of bright shrinking loops and dark voids along the same line of sight suggests otherwise [Savage et al., 2012].
2. the mismatch in size between dark voids and shrinking loops, i.e., the loop is consistently thinner than the void [Savage & McKenzie, 2011].

The above discrepancies have motivated Savage et al. [2012] to reinterpret dark voids as wakes of shrinking loops. But it is unclear in this reinterpretation what results in rarefaction behind shrinking loops, which move at one tenth of the Alfvén speed. Moreover, our observation of a dark void moving within the VCS indicates that this particular void must be located significantly higher than the loop retracting from the cusp, rather than trail immediately behind the loop.

As a variation of the traditional interpretation, we suggest that the scenario proposed for plasma blobs observed in VCSs (Figure 10) is also applicable to dark voids observed in SADs, because they are very similar to each other in that they both 1) move along the VCS (Figure 9), 2) show wave-like signatures (see Figure 7 and Verwichte et al. 2005), and 3) are closely related to field line shrinkage (see Figure 7 and Savage et al. 2012). In this variation, we conjecture that the dark void could be a mini flux rope staying at the top of the highly-stretched reconnected flux tube until it arrives at the cusp region with the retraction of the stretched field, where the void shrinks and disappears as the twist within the mini flux rope is transported away via Alfvén waves (§3.3). This can accommodate the co-existence of bright shrinking loops and dark voids along the same line of sight, and naturally accounts for their difference in observational appearance. Stretched by reconnection outflows, the flux rope may take the tadpole-like shape as observed in SADs [Linton & Longcope, 2006]. As a comparison, the dark void in the traditional interpretation would be identified with the cross section of the shrinking loop which is evolving on Stage 3 in Figure 10.

After identifying both plasma blobs in the VCS and dark voids in SADs as mini flux ropes, we may further argue that a flux rope could appear either dark or bright, depending not only on its own property but on the external environment as well. First of all, a stationary flux rope may appear dark when it contains higher internal magnetic pressure but less dense plasma than external to maintain the total pressure. This is basically the same argument for the identification of dark voids as cross-sections of shrinking loops in the first place [e.g., McKenzie & Savage, 2009]. Moreover, the evolution of a mini flux rope can be regarded as an adiabatic process if it moves fast enough compared with the sound speed of 10 MK plasma at the VCS ($c_s = \sqrt{\gamma k_B T / \mu m_p} \simeq 330 \text{ km s}^{-1}$, where $\mu = 1.27$ is the mean molecular weight). Therefore, if it forms relatively high in the corona, as most SADs

do during the gradual phase, a downward-moving mini flux rope would appear as a dark void when it is seen in the lower corona, because it is more tenuous than its surroundings, whereas an upward-moving mini flux rope would appear in emission when it is seen in the higher corona, because it is denser than its surroundings. On the other hand, one expects to see similar brightness as its surroundings, when a flux rope forms relatively locally, or moves slowly enough so that it has sufficient time to respond to the external pressure. This may account for a wide spread of the signal intensity of SADs from dark to bright [McKenzie, 2000; Savage & McKenzie, 2011].

This hypothesis is appealing as it unites plasma blobs, dark voids and field line shrinkage into a single picture. Of course, further testing against more observations is needed.

Acknowledgments. The author is grateful to the *SDO*, *STEREO*, *RHESSI* and Nobeyama teams for the free access to the data and the development of the data analysis software. This work was supported by the Thousand Young Talents Program of China, NSFC 41222031 and NSF AGS-1153226, and partially supported by NSFC 41131065 and 41121003, 973 key project 2011CB811403, CAS Key Research Program KZZD-EW-01-4, the fundamental research funds for the central universities WK2080000031.

References

- Amari T., Luciani J. F., Mikic Z., Linker J., 2000, *Astrophys. J. Lett.*, 529, L49
- Asai A., Yokoyama T., Shimojo M., Shibata K., 2004, *Astrophys. J. Lett.*, 605, L77
- Aschwanden M. J., 2006, *Physics of the Solar Corona*, 2nd edn. Springer
- Aulanier G., DeLuca E. E., Antiochos S. K., McMullen R. A., Golub L., 2000, *Astrophys. J.*, 540, 1126
- Bemporad A., Poletto G., Suess S. T., Ko Y., Schwadron N. A., Elliott H. A., Raymond J. C., 2006, *Astrophys. J.*, 638, 1110
- Chen P. F., Shibata K., 2000, *Astrophys. J.*, 545, 524
- Ciaravella A., Raymond J. C., 2008, *Astrophys. J.*, 686, 1372
- Ciaravella A., Raymond J. C., Li J., Reiser P., Gardner L. D., Ko Y., Fineschi S., 2002, *Astrophys. J.*, 575, 1116
- Fletcher L., Hudson H. S., 2008, *Astrophys. J.*, 675, 1645
- Forbes T. G., 1986, *Astrophys. J.*, 305, 553
- Forbes T. G., Acton L. W., 1996, *Astrophys. J.*, 459, 330
- Forbes T. G., Priest E. R., 1995, *Astrophys. J.*, 446, 377
- Hurford G. J., Schmahl E. J., Schwartz R. A., Conway A. J., Aschwanden M. J., Csillaghy A., Dennis B. R., Johns-Krull C., Krucker S., Lin R. P., McTiernan J., Metcalf T. R., Sato J., Smith D. M., 2002, *Solar Phys.*, 210, 61
- Innes D. E., McKenzie D. E., Wang T., 2003, *Solar Phys.*, 217, 247
- Ji H., Huang G., Wang H., 2007, *Astrophys. J.*, 660, 893
- Ji H., Huang G., Wang H., Zhou T., Li Y., Zhang Y., Song M., 2006, *Astrophys. J. Lett.*, 636, L173
- Ji H., Wang H., Goode P. R., Jiang Y., Yurchyshyn V., 2004, *Astrophys. J. Lett.*, 607, L55

- Joshi B., Veronig A., Cho K.-S., Bong S.-C., Somov B. V., Moon Y.-J., Lee J., Manoharan P. K., Kim Y.-H., 2009, *Astrophys. J.*, 706, 1438
- Karpen J. T., Antiochos S. K., Devore C. R., 1995, *Astrophys. J.*, 450, 422
- Karpen J. T., Antiochos S. K., DeVore C. R., 2012, *Astrophys. J.*, 760, 81
- Khan J. I., Bain H. M., Fletcher L., 2007, *Astron. Astrophys.*, 475, 333
- Ko Y., Raymond J. C., Lin J., Lawrence G., Li J., Fludra A., 2003, *Astrophys. J.*, 594, 1068
- Ko Y.-K., Raymond J. C., Vršnak B., Vujčić E., 2010, *Astrophys. J.*, 722, 625
- Kopp R. A., Pneuman G. W., 1976, *Solar Phys.*, 50, 85
- Lemen J. R., Title A. M., Akin D. J., et al., 2012, *Solar Phys.*, 275, 17
- Lin J., 2004, *Solar Phys.*, 222, 115
- Lin J., Forbes T. G., 2000, *J. Geophys. Res.*, 105, 2375
- Lin J., Ko Y., Sui L., Raymond J. C., Stenborg G. A., Jiang Y., Zhao S., Mancuso S., 2005, *Astrophys. J.*, 622, 1251
- Linker J. A., Mikić Z., Lionello R., et al., 2003, *Phys. Plasmas*, 10, 1971
- Linton M. G., Longcope D. W., 2006, *Astrophys. J.*, 642, 1177
- Liu R., Lee J., Wang T., Stenborg G., Liu C., Wang H., 2010, *Astrophys. J. Lett.*, 723, L28
- Liu R., Wang H., Alexander D., 2009, *Astrophys. J.*, 696, 121
- Liu R., Wang T.-J., Lee J., Stenborg G., Liu C., Park S.-H., Wang H.-M., 2011, *Research in Astronomy and Astrophysics*, 11, 1209
- Liu W., Chen Q., Petrosian V., 2013, *Astrophys. J.*, 767, 168
- Liu W., Jiang Y. W., Liu S., Petrosian V., 2004, *Astrophys. J. Lett.*, 611, L53
- Liu W., Petrosian V., Dennis B. R., Holman G. D., 2009, *Astrophys. J.*, 693, 847
- Longcope D. W., Bradshaw S. J., 2010, *Astrophys. J.*, 718, 1491
- Lynch B. J., Antiochos S. K., DeVore C. R., Luhmann J. G., Zurbuchen T. H., 2008, *Astrophys. J.*, 683, 1192
- McKenzie D. E., 2000, *Solar Phys.*, 195, 381
- McKenzie D. E., Hudson H. S., 1999, *Astrophys. J. Lett.*, 519, L93
- McKenzie D. E., Savage S. L., 2009, *Astrophys. J.*, 697, 1569
- O'Dwyer B., Del Zanna G., Mason H. E., Weber M. A., Tripathi D., 2010, *Astron. Astrophys.*, 521, A21
- Patsourakos S., Vourlidis A., Stenborg G., 2013, *Astrophys. J.*, 764, 125
- Pesnell W. D., Thompson B. J., Chamberlin P. C., 2012, *Solar Phys.*, 275, 3
- Raymond J. C., Ciaravella A., Dobrzycka D., Strachan L., Ko Y., Uzzo M., Raouafi N., 2003, *Astrophys. J.*, 597, 1106
- Reeves K. K., Linker J. A., Mikić Z., Forbes T. G., 2010, *Astrophys. J.*, 721, 1547
- Reeves K. K., Seaton D. B., Forbes T. G., 2008, *Astrophys. J.*, 675, 868
- Roussev I. I., Forbes T. G., Gombosi T. I., et al., 2003, *Astrophys. J. Lett.*, 588, L45
- Savage S. L., McKenzie D. E., 2011, *Astrophys. J.*, 730, 98
- Savage S. L., McKenzie D. E., Reeves K. K., 2012, *Astrophys. J. Lett.*, 747, L40
- Savage S. L., McKenzie D. E., Reeves K. K., Forbes T. G., Longcope D. W., 2010, *Astrophys. J.*, 722, 329
- Sheeley Jr. N. R., Warren H. P., Wang Y.-M., 2004, *Astrophys. J.*, 616, 1224
- Shiota D., Yamamoto T. T., Sakajiri T., Isobe H., Chen P.-F., Shibata K., 2003, *Pub. Astron. Soc. Japan*, 55, L35
- Somov B. V., Kosugi T., 1997, *Astrophys. J.*, 485, 859
- Sui L., Holman G. D., 2003, *Astrophys. J. Lett.*, 596, L251
- Sui L., Holman G. D., Dennis B. R., 2004, *Astrophys. J.*, 612, 546
- Svestka Z. F., Fontenla J. M., Machado M. E., Martin S. F., Neidig D. F., 1987, *Solar Phys.*, 108, 237
- Takasao S., Asai A., Isobe H., Shibata K., 2012, *Astrophys. J. Lett.*, 745, L6
- Temmer M., Veronig A. M., Kontar E. P., Krucker S., Vršnak B., 2010, *Astrophys. J.*, 712, 1410
- Veronig A. M., Karlický M., Vršnak B., et al., 2006, *Astron. Astrophys.*, 446, 675
- Verwichte E., Nakariakov V. M., Cooper F. C., 2005, *Astron. Astrophys.*, 430, L65
- Vršnak B., Temmer M., Veronig A., Karlický M., Lin J., 2006, *Solar Phys.*, 234, 273
- Warren H. P., O'Brien C. M., Sheeley Jr. N. R., 2011, *Astrophys. J.*, 742, 92
- Webb D. F., Burkepile J., Forbes T. G., Riley P., 2003, *Journal of Geophysical Research (Space Physics)*, 108, 1440
- Wuelser J.-P., Lemen J. R., Tarbell T. D., et al., 2004, in S. Fineschi & M. A. Gummin ed., *Society of Photo-Optical Instrumentation Engineers (SPIE) Conference Series*, Vol. 5171, *Telescopes and Instrumentation for Solar Astrophysics*. pp 111–122
- Zhang J., Dere K. P., 2006, *Astrophys. J.*, 649, 1100
- Zhang J., Dere K. P., Howard R. A., Kundu M. R., White S. M., 2001, *Astrophys. J.*, 559, 452